Hindawi
Advances in Materials Science and Engineering
Volume 2021, Article ID 5892788, 14 pages
https://doi.org/10.1155/2021/5892788

Research Article

Seismic Behavior of Elliptical Concrete-Filled Steel Tubular Columns under Combined Axial Compression and Cyclic Lateral Loading

YouWu Xu,[1] **Jian Yao**,[1] **Feng Hu**,[2] **Ying Zhou**,[1] **and Shuai Jiang**[1]

[1]*College of Civil Engineering and Architecture, Quzhou University, Quzhou 324000, China*
[2]*Ningbo Urban Planning and Design Institute, Ningbo 315000, China*

Correspondence should be addressed to YouWu Xu; xuyouwu@zju.edu.cn

Received 11 August 2021; Revised 9 December 2021; Accepted 10 December 2021; Published 31 December 2021

Academic Editor: Rotana Hay

Copyright © 2021 YouWu Xu et al. This is an open access article distributed under the Creative Commons Attribution License, which permits unrestricted use, distribution, and reproduction in any medium, provided the original work is properly cited.

Elliptical concrete-filled steel tubular (CFST) column is a new form of CFST columns, consisting of an outer elliptical tube filled with concrete. Although the study on mechanical performance of the elliptical CFST members is receiving more and more attention, they have been limited to static behavior. Against this background, an experimental study on elliptical CFST columns was carried out under combined axial compression and cyclic lateral loading. The failure modes, hysteretic curves, skeleton curves, load carrying capacity, deformability, stiffness degradation, and energy dissipation ability was obtained and discussed. The test results indicated that the elliptical CFST columns possess excellent seismic performance and ductility. Valuable experimental data were provided for the formulation of the theoretical hysteresis model of the elliptical CFST columns.

1. Introduction

Concrete-filled steel tubular (CFST) columns have been widely used in modern construction due to their high strength, high ductility, and ease of construction [1]. In the past few decades, a lot of research on the performance and design of CFST members under various loading condition [2] have been published. As a new section form of CFST, elliptical CFST (Figure 1) has attracted the attention of many scholars from home and abroad. In recent years, research has been carried out on the mechanical behavior and design method of elliptical CFST.

Experimental study on elliptical CFST stub columns with different thickness and concrete strength subjected to axial loading have been conducted by Yang et al. [3], Zhao and Packer [4], Jamaluddin et al. [5], Chan et al. [6], and Cai et al. [7]. They proved the merits of elliptical CFST stub columns, but all the specimens they tested have the same aspect ratio ($a/b = 2.0$). With the development of manufacturing technology, the elliptical steel tube with various aspect ratios is available in construction practice. Thus, elliptical CFST stub columns with an aspect ratio from 1.0 to 2.5 were tested by Zha et al. [8], Uenaka [9], Yi and Young [10], Liu et al. [11], and Xu et al. [12]. All the test results confirmed that the confinement effect decreases significantly with the increasing aspect ratio. Simultaneously, the eccentrically compressed columns were also investigated by Sheehan et al. [13], Zha et al. [14], Ren et al. [15], Qiu [16], and Yang et al. [17]. On the other side, systematic finite element analysis [18–22] was performed to simulate elliptical CFST columns subjected to concentric and eccentric axial compression. However, these studies mainly focused on static behavior, and research on their seismic behavior is very limited, which may hamper the application of elliptical CFST members in the seismic region. To the best of the authors' knowledge, the pseudostatic tests on 5 specimens with an aspect ratio of 2.0 conducted by Ma [23] proved the influence of concrete cube strength and axial compression ratio on the seismic behavior of elliptical CFST columns. Fang et al. [24] further considered the thickness of the elliptical steel tube, axial compression ratio, and the loading direction of horizontal loading; nevertheless, the aspect ratio of the specimens was

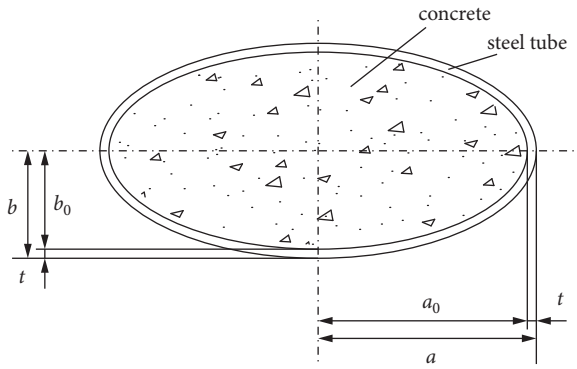

Figure 1: Cross-section of elliptical CFST.

also limited to 2.0. Consequently, the studies on the seismic behavior of elliptical CFST columns with an aspect ratio of a wider range is urgently needed.

In this study, 13 elliptical CFST columns tested under combined axial compression and cyclic lateral loading, the failure mode, carrying capacity, deformation capacity, hysteretic curve, and energy dissipation capacity of the specimens are discussed in detail. The experiment results may provide the reference to the analysis and application of elliptical CFST columns in the seismic area.

2. Experimental Program

2.1. Test Specimens. A total of 13 specimens were tested under combined constant axial compression and cyclic lateral loading through either the long or short axis. The key parameters were aspect ratio a/b, concrete cube strength f_{cu}, axial compression ratio n, and slenderness ratio λ_{sc}, which is expressed as column height h. As shown in Figure 2, each specimen consists of an elliptical CFST column, a top end-plate with a thickness of 20 mm, a series of stiffeners with a thickness of 10 mm welded to the top end-plate and the column, and a 30 mm thick bottom end-plate. The height of welding is $h_f = 6$ mm. According to the insite condition, rolling support on the vertical jack was not so smooth for sliding. So, the stiffeners were not used at the column base to achieve an equivalent calculation length to the cantilever component.

Table 1 provides the details of the 13 specimens, in which a is the length of semimajor axis, b is the length of semiminor axis, t is the thickness of the steel tube, and h is the height of the specimen. The specimen was named by the key parameters as follows: the aspect ratio-concrete cube strength-axial ratio. The letters m and l added at the end denote the medium (2050 mm) and the longest columns (2550 mm), and b for bending around the major axis. If there are no letters at the end, it means 1300 mm height and bending around the minor axis. The axial ratio was determined by equation (1), where N_d is the constant axial compression subjected by the specimen, A_c and A_s are the measured cross-sectional areas of the steel and concrete, respectively, and f_{co} and f_y are the cylinder strength, converted from the measured concrete cube strength [25] of concrete and yield strength of steel.

$$n = \frac{N_d}{\left(f_{co}A_c + f_y A_s\right)}. \quad (1)$$

The elliptical steel tubes were cold-formed from the welded circular tubes (Figure 3). The material test of the steel tube was conducted according to [26], and the yield stress f_y and elastic modulus E_s of the steel tubes were obtained from the tensile coupon tests (Figure 4), as given in Table 1. Concrete grade C45, C60, C75, and C100 was used, and the mix proportions and tested cube strength are given in Table 2 and Table 1, respectively.

2.2. Instrument and Loading Procedure. As shown in Figure 5, the specimens were placed and tested within a reaction testing frame. The axial load was applied by a vertical hydraulic jack which is movable in the horizontal direction. The horizontal electrohydraulic servoactuator with a load capacity of 1000 kN and a stroke of 200 mm was used to apply the horizontal load. The push direction is defined as positive direction.

Eight LVDTs were used to measure the critical displacements. LVDT 1-2 were used to measure the translational movement of the foundation beam, LVDT 3-4 were used to measure the rotation of bottom end-plate. LVDT 5-6 were used to measure the columns end shortening within the 200 mm range. LVDT 7-8 were used to measure the translational displacement of the top of the column.

The loading procedure included three steps. A 30% of the designed vertical load was first preloaded to check the testing system. Then, the designed vertical load was applied and kept constant. Finally, the horizontal load was applied quasistatically following the JGJ/T standard loading protocol (JGJ/T 101-2015) [27], which is shown in Figure 6. Each of the first three levels of amplitude (0.25 Δ_y, 0.5 Δ_y, and 0.75 Δ_y) was repeated only for one cycle, followed by three cycles at the rest levels of amplitude (1 Δ_y,2 Δ_y,4 Δ_y, 6 Δ_y, 8 Δ_y. . .). The loading procedure was stopped when the horizontal load degraded to 85% of the peak load.

3. Test Results and Discussion

3.1. Failure Mode. Two typical failure modes were observed from the experimental results, namely, local buckling near the bottom end-plate and the fracture of the steel tube (Table 3 and Figure 7). For the local buckling failure mode, the outward bulges were observed at about 45 mm distance from the bottom end-plate. The bulges became more and more evident with the increase in the horizontal loading amplitude. Finally, the "elephant foot" failure mechanism was formed. For the fracture failure mode, the fracture occurred in the steel tube but not in the weld. It is mainly caused by stress concentration related to the heat-affected zone of the weld. The lack of stiffeners causes massive tension in the bottom of the steel tube, and it may be another reason for the fracture. More experiments or finite element analyses are needed to reveal the convinced reason.

In order to further investigate the damage condition of the concrete, end part of the steel tube was cut after the

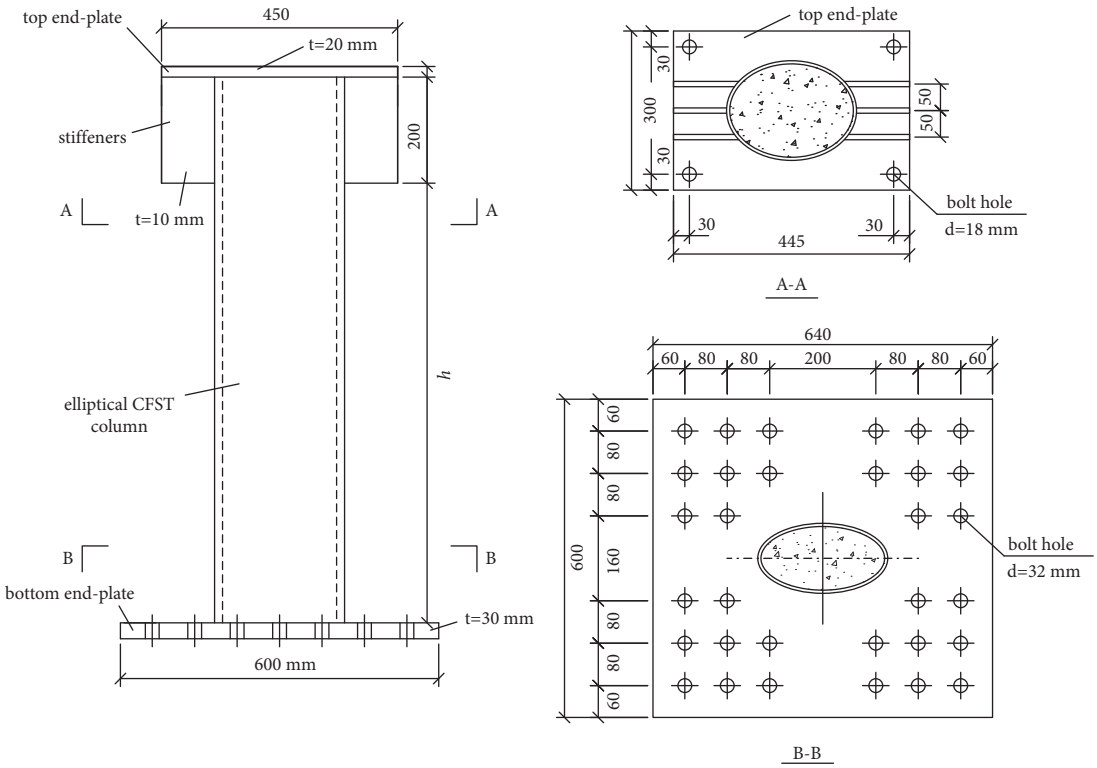

Figure 2: Details of the specimens.

Table 1: Measured information of the specimens.

Specimen	$2a$ (mm)	$2b$ (mm)	t (mm)	h (mm)	f_y (MPa)	E_s (MPa)	f_{cu} (MPa)
E1.0-C45-0.2	244.81	244.81	5.88	1300.00	334	190650	45.31
E1.3-C45-0.2	243.99	187.25	5.89	1300.00	370	214500	45.31
E1.8-C45-0.2	243.61	132.86	6.06	1300.00	389	214600	45.31
E2.3-C45-0.2	244.45	103.92	5.86	1300.87	409	203780	45.31
E1.8-C60-0.2	243.55	133.85	6.07	1300.57	389	214600	69.97
E1.8-C75-0.2	243.68	133.83	6.12	1300.63	389	214600	76.01
E1.8-C100-0.2	243.20	132.41	6.09	1302.67	389	214600	92.45
E1.8-C45-0.1	243.60	132.51	6.09	1305.50	389	214600	45.31
E1.8-C45-0.3	243.45	132.99	6.07	1300.27	389	214600	45.31
E1.8-C45-0.2m	243.52	133.04	6.04	2050.46	389	214600	45.31
E1.8-C45-0.2l	243.51	132.86	6.07	2552.31	389	214600	45.31
E1.8-C45-0.2b	243.73	132.37	6.08	1300.00	389	214600	45.31
E1.8-C45-0.3b	243.77	132.85	6.03	1300.33	389	214600	45.31

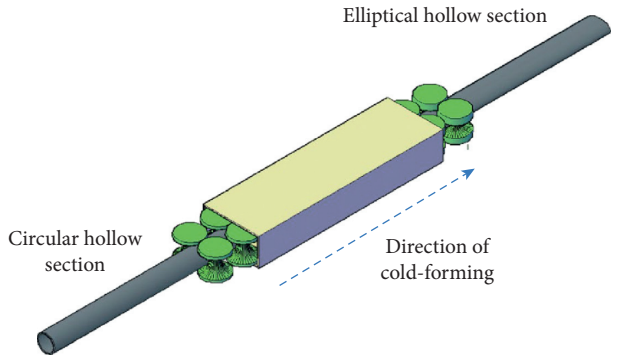

Figure 3: Cold-forming process (Chan et al. [6]).

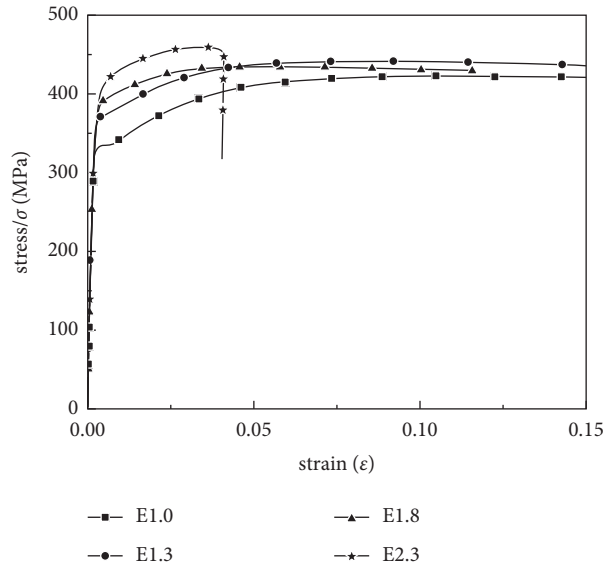

Figure 4: Stress-strain relationships of elliptical steel tubes.

Table 2: Mix proportions of the concrete (kg/m^3).

Concrete grade	Cement	Water	Fines	Coarse	Fly ash	Water reducer	Expansion mixture
C45	363	191	790	851	176	0	55
C60	355	177	740	935	109	10	54
C75	375	150	720	1025	115	12	58
C100	390	132	700	1050	102	16	60

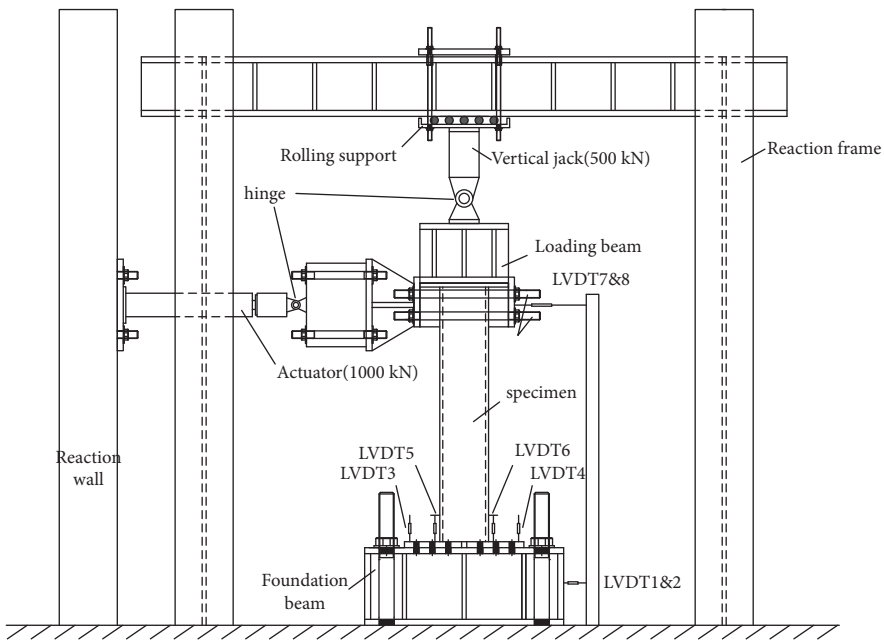

Figure 5: Test setup and instrumentation.

experiments, as shown in Figure 8. The concrete was crushed on both sides of the loading direction, and several minor cracks were observed.

3.2. Hysteretic and Skeleton Curves. The horizontal force-displacement responses of the ECFST beam-column specimens are shown in Figure 9. The test results showed that the

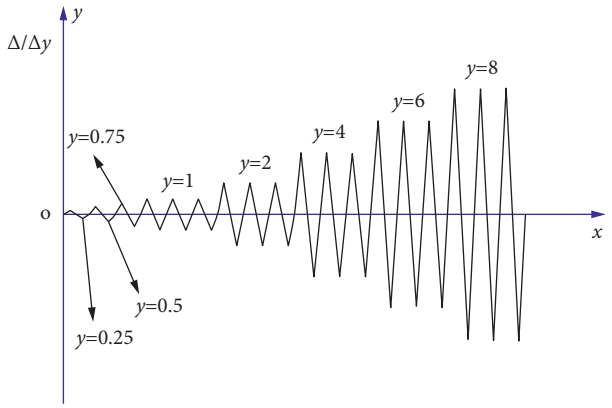

Figure 6: Horizontal loading procedure.

Table 3: Failure modes of the specimens.

Failure modes	Specimens
Local buckling	E1.3-C45-0.2, E1.8-C45-0.2, E1.8-C75-0.2, E1.8-C100-0.2,E1.8-C45-0.1, E1.8-C45-0.3, E1.8-C45-0.2m, E1.8-C45-0.2l, E1.8-C45-0.2b, E1.8-C45-0.3b
Fracture of the steel tube	E2.3-C45-0.2, E1.8-C60-0.2

*The loading procedure of E1.0-C45-0.2 was not completed due to the abrupt failure of the instrument.

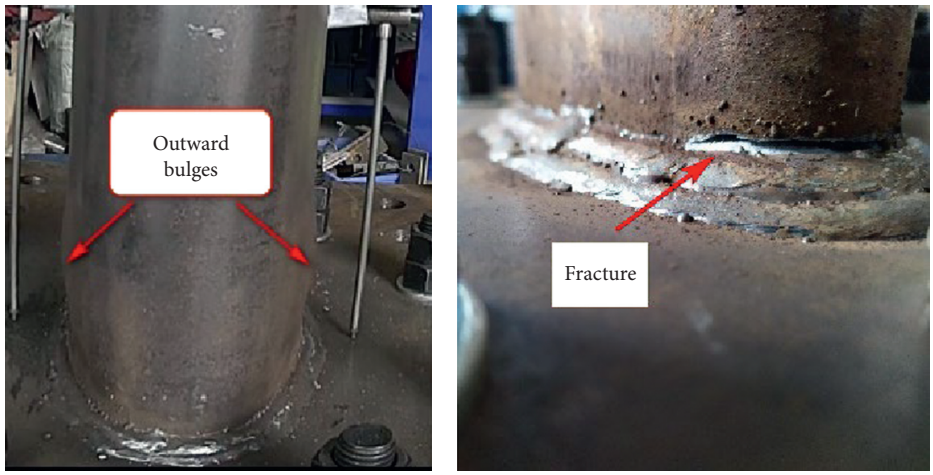

(a) (b)

Figure 7: Typical failure modes of the specimens. (a) Local buckling. (b) Fracture of the steel tube.

hysteretic curves were chubbiness without pinching, which reveals the high-energy dissipation capacity. The hysteresis remains stable as the amplitude increase, and the three hysteresis loops at the same amplitude is almost the same at the earlier stage. When the applied load reaches the ultimate horizontal force P_u, degradation of the hysteresis begins to be seen, in which case the loops became smaller as the cycle number increases.

Skeleton curves are shown in Figure 10 which were constructed by tracing the maximum loads at varying amplitudes. The skeleton curves consist of three stages, namely, the initial elastic ascending stage, nonlinear elastic-plastic ascending stage, and postpeak descending stage. As expected, concrete strength and axial compression ratio has a little effect on the initial stiffness, increasing the concrete strength tends to increase the ultimate load and speed up the

Figure 8: Typical damage mode of the concrete.

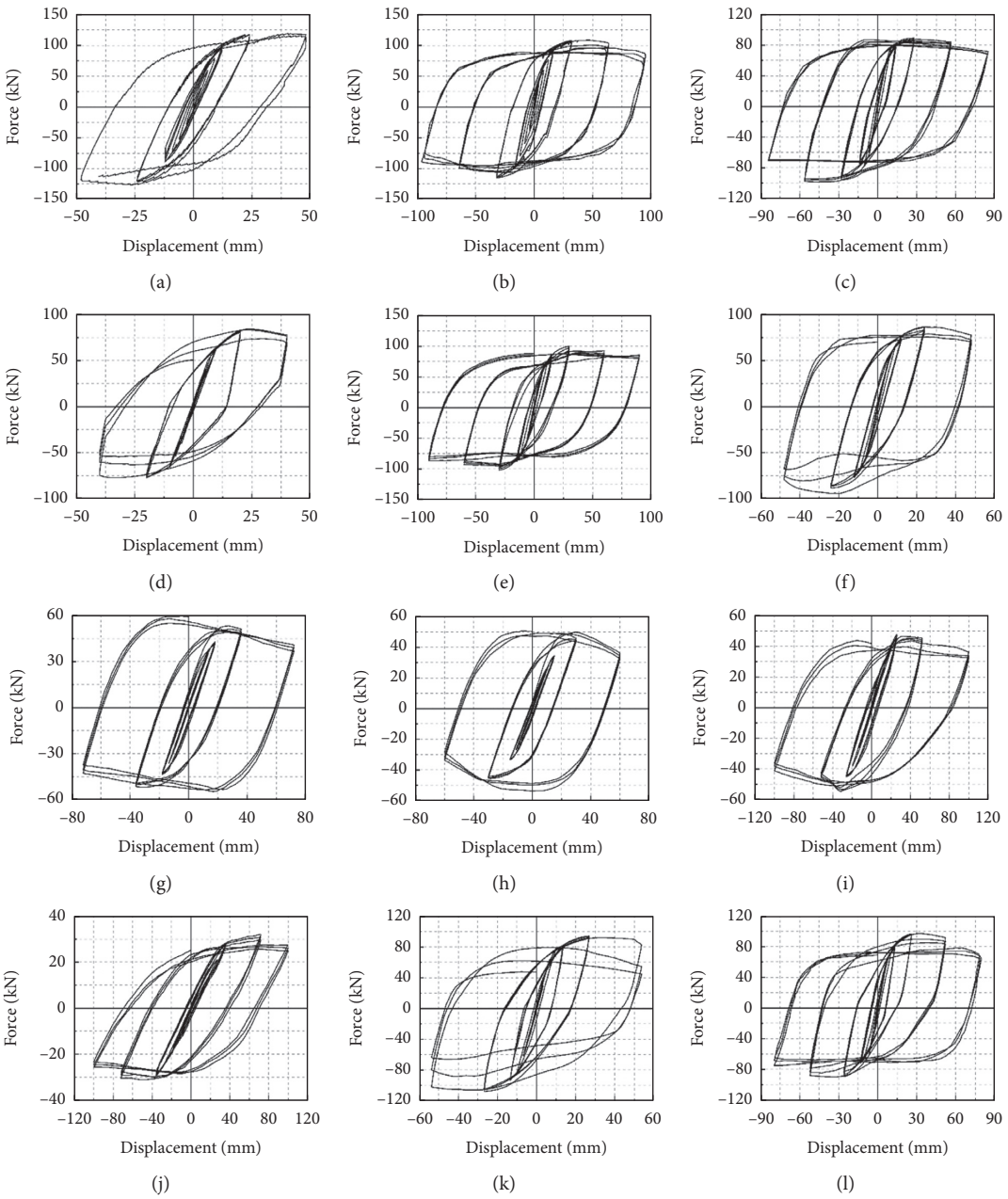

Figure 9: Continued.

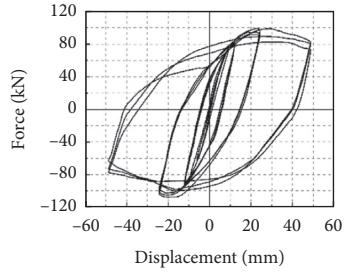

Figure 9: Horizontal force-displacement responses of the test specimens. (a) E1.0-c45-0.2. (b) E1.3-c45-0.2. (c) E1.8-c45-0.2. (d) E2.3-c45-0.2. (e) E1.8-c45-0.1. (f) E1.8-c45-0.3. (g) E1.8-c45-0.2b. (h) E1.8-c45-0.3b. (i) E1.8-c45-0.2m. (j) E1.8-c45-0.2l. (k) E1.8-c60-0.2. (l) E1.8-c75-0.2. (m) E1.8-c100-0.2.

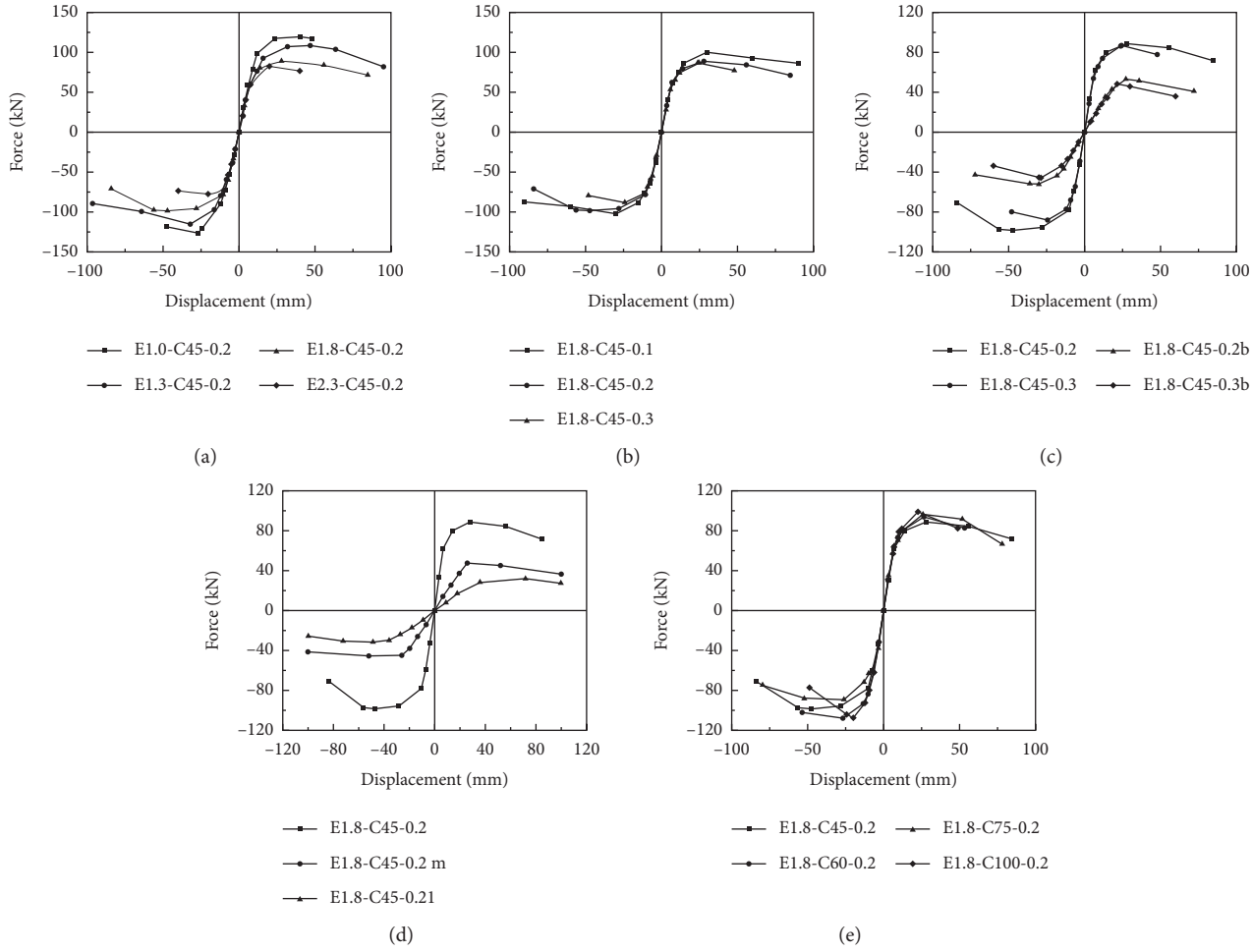

Figure 10: Skeleton cures of test specimens. (a) Variation of aspect ratio. (b) Variation of axial compression ratio. (c) Variation of bending axis. (d) Variation of slenderness ratio. (e) Variation of concrete strength.

degradation progress, and increasing the axial compression ratio is likely to decrease the ultimate load and speed up the degradation progress. The initial stiffness and ultimate load decreases with the increase of aspect ratio and slenderness ratio, and the load drops faster as the aspect ratio increases and slenderness decreases. Major axis bending leads to the larger initial stiffness and ultimate load than minor axis bending, but it results in the more abrupt degradation.

3.3. Bearing Capacity and Ductility. The ductility of a beam-column is generally regarded as the deformation capacity which is defined as the ability to sustain plastic deformations before its failure. The most commonly used parameter is the ductility index μ and can be expressed as

$$\mu = \frac{\Delta_u}{\Delta_y}, \tag{2}$$

where Δ_{ul} and Δ_y are the ultimate displacement and yield displacement, respectively, Δ_{ul} is taken as the displacement at a 15% reduction in the ultimate load [28], and Δ_y is calculated from the skeleton curves using the average calculation of the geometric graphic method, equivalent elastoplastic energy method, and R. Park method [29], which are three common methods used to define the yield strength/load and yield displacement/drift. The ultimate load P_u, ultimate displacement Δ_{ul} obtained from the skeleton curves, and the calculated yield load P_y, yield displacement Δ_y are given in Table 4.

As given in Table 4, the ductility index of most specimens is greater than 3.0, indicating a highly ductile performance. The ductility index decreases with the increase of aspect ratio, axial compression ratio, slenderness ratio, and concrete strength. Major axis bending specimen has a greater ductility than that of minor axis bending specimen. The aspect ratio seems to have moderate influence on the ductility index.

3.4. Stiffness Degradation. As guided in the JGJ/T code (JGJ/T 101-2015, 2015), the average stiffness can be obtained from the horizontal load-displacement hysteretic curves, which can be expressed as

$$K_i = \frac{\sum_{j=1}^{m}\left(\left|(+)P_{i,j}\right| + \left|(-)P_{i,j}\right|\right)}{\sum_{j=1}^{m}\left(\left|(+)\Delta_{i,j}\right| + \left|(-)\Delta_{i,j}\right|\right)}, \tag{3}$$

where K_i is the average stiffness of the specimen at the i^{th} amplitude, $P_{i,j}$ is the maximum load of the j^{th} cycle at the i^{th} amplitude, $\Delta_{i,j}$ is the maximum displacement of the j^{th} cycle at the i^{th} amplitude, and (+) and (−) mean the positive and negative position, respectively.

Figure 11 shows the relationship of the average stiffness with horizontal displacement; it illustrates the stiffness degradation with increasing lateral displacement, which is highly correlated with the development concrete cracks. In all test specimens, the stiffness degradation is significant before the displacement reaches to $2\Delta_y$; as the displacement continues to increase, the stiffness degradation continues at a lower and continually decreasing rate. The aspect ratio, axial compression ratio, and concrete strength have a little effect on the stiffness degradation. The stiffness reduces faster when the specimen is less slender, and the stiffness degradation rate of minor axis bending specimen is lower than that of major axis bending specimen.

3.5. Energy Dissipation Capacity. The energy dissipation per cycle, E_i, is the area enveloped by each hysteretic loop [24, 30, 31]. Figure 12 shows the accumulated energy dissipation $\sum E_i$ of the 13 test specimens. As seen from the table, negligible energy dissipation is observed before the specimen reached the yield point, before which the specimens sustain limited plastic deformation. The energy dissipation starts to accumulate with the accumulated plastic deformation. The ultimate accumulated energy dissipation reflects the energy dissipation performance of the test specimens. As shown in Figure 12, specimens with a smaller aspect ratio, lower concrete strength, smaller axial compression ratio, and smaller slenderness ratio possess better energy dissipation capacity, and major axis bending specimens have a better performance on the energy dissipation quality than that of minor axis bending specimens.

4. Simplified Model of Force-Displacement Hysteretic Curve

4.1. Introduction of the Simplified Model. A kind of trilinear model is suggested by Han and Yang [32] and Han [2] to simplify the horizontal load P versus horizontal displacement Δ hysteretic relationship. A schematic view of the simplified force-displacement hysteretic relationship is shown in Figure 13. The key parameters of the model are listed as follows.

(1) Elastic stiffness K_e is given by

$$K_{\text{e}} = \frac{3EI}{l_0^3}, \qquad EI = E_{\text{s}}I_{\text{s}} + 0.6E_{\text{c}}I_{\text{c}}. \tag{4}$$

Here, l_0 is the effective length, E_c is the elastic modulus of concrete, which is expressed as $E_c = 4730\sqrt{f_{\text{co}}}$ [33], and I_s and I_c are the moment of inertia for the outer steel cross-section and inner concrete cross-section.

(2) The ultimate strength P_u and corresponding displacement Δ_u can be given by

$$P_u = \begin{cases} \dfrac{1.05a_1M_y}{h} & 1 < \xi_c \le 4 \\ \dfrac{a_1\left(0.2\xi_c + 0.85\right)M_y}{h} & 0.2 < \xi_c \le 1 \end{cases},$$

$$a_1 = \begin{cases} 0.96 - 0.002\xi_c & 0 \le n \le 0.3 \\ \left(1.4 - 0.34\xi_c\right)n + 0.1\xi_c + 0.54 & 0.3 < n < 1 \end{cases},$$

$$\Delta_u = \frac{6.74\left[(\ln r)^2 - 1.08\ln r + 3.33\right]f_1(n)}{8.7 - s}\cdot\frac{P_u}{K_e},$$

$$f_1(n) = \begin{cases} 1.336n^2 - 0.044n + 0.8040 & 0 \le n \le 0.5 \\ 1.126 - 0.02n & 0.5 < n < 1 \end{cases} \tag{5}$$

Table 4: Load bearing capacity and ductility of test specimens.

Specimens		P_u (kN)	Δ_{ul} (mm)	P_y (kN)	Δ_y (mm)	μ
E1.0-C45-0.2	Positive direction	119.35	[a]>48.05	103.02	14.78	>3.27
	Negative direction	126.49	[a]>48.06	107.02	18.88	>2.55
	Average	122.92	[a]>48.06	105.02	16.83	>2.91
E1.3-C45-0.2	Positive direction	108.43	80.30	94.17	17.47	>4.60
	Negative direction	115.05	69.00	99.65	18.15	3.81
	Average	111.74	74.65	96.91	17.81	4.21
E1.8-C45-0.2	Positive direction	89.03	75.72	75.95	12.37	6.14
	Negative direction	98.48	70.70	81.74	14.16	5.05
	Average	93.75	73.21	78.84	13.26	5.59
E2.3-C45-0.2	Positive direction	84.53	40.06	71.07	13.14	3.05
	Negative direction	77.35	40.08	67.73	11.59	3.46
	Average	80.94	40.07	69.40	12.37	3.26
E1.8-C60-0.2	Positive direction	94.22	53.66	80.44	12.35	4.38
	Negative direction	108.08	53.66	93.58	13.96	3.85
	Average	101.15	53.66	87.01	13.16	4.12
E1.8-C75-0.2	Positive direction	97.09	61.51	81.42	14.00	4.41
	Negative direction	89.78	76.72	72.22	13.87	5.61
	Average	93.44	69.11	76.82	13.93	5.01
E1.8-C100-0.2	Positive direction	99.32	45.88	84.14	13.18	3.48
	Negative direction	107.70	35.71	94.10	13.00	2.75
	Average	103.51	40.79	89.12	13.09	3.12
E1.8-C45-0.1	Positive direction	100.10	90.05	85.01	14.75	6.12
	Negative direction	102.10	90.01	86.94	14.77	6.11
	Average	101.10	90.03	85.97	14.76	6.11
E1.8-C45-0.3	Positive direction	86.70	48.01	74.22	12.27	3.92
	Negative direction	94.50	45.54	79.93	13.36	3.41
	Average	90.60	46.77	77.08	12.82	3.66
E1.8-C45-0.2m	Positive direction	47.58	78.14	45.97	25.00	3.13
	Negative direction	54.64	49.83	51.93	30.00	1.66
	Average	51.11	63.99	48.95	27.50	2.39
E1.8-C45-0.2l	Positive direction	32.00	99.78	28.82	40.19	2.48
	Negative direction	31.20	95.19	29.13	35.50	2.68
	Average	31.60	97.49	28.97	37.85	2.58
E1.8-C45-0.2b	Positive direction	54.70	56.68	48.00	22.57	2.51
	Negative direction	52.00	66.26	45.94	21.39	3.10
	Average	53.35	61.47	46.97	21.98	2.81
E1.8-C45-0.3b	Positive direction	48.50	44.35	47.08	21.00	2.11
	Negative direction	45.60	46.70	39.63	22.06	2.12
	Average	47.05	45.52	43.36	21.53	2.12

[a]The loading procedure of E1.0-C45-0.2 was not completed due to the abrupt failure of the instrument.

Here, $\xi_c = A_s f_y / A_c f_{ck} = \alpha \cdot f_y / f_{ck}$ is the steel confinement factor, in which f_{ck} is the prism compressive strength of concrete [25], $\alpha = A_s/A_c$ is the steel ratio, $r = \lambda_{sc}/40$, and $s = f_y/345$.

(3) Stiffness of the descending stage K_T is given by

$$K_T = \frac{0.03 \cdot f_2(n) \cdot f(r,\alpha) \cdot K_e}{c^2 - 3.39c + 5.41},$$

$$f_2(n) = \begin{cases} 3.043n - 0.21 & 0 \le n \le 0.7, \\ 1.57 + 0.5n & 0.7 < n < 1, \end{cases} \quad (6)$$

$$f(r,\alpha) = \begin{cases} (8\alpha - 8.6)r + 6\alpha + 0.9 & r \le 1, \\ (15\alpha - 13.8)r + 6.1 - \alpha & r > 1, \end{cases}$$

where $c = f_{cu}/60$.

4.2. Comparison of the Simplified Model with Tested Curve. To verify the validity of the above formulas, the force-displacement hysteretic relationships calculated with the simplified model were compared with those obtained from the experiment, as shown in Figure 14. It is proved that the simplified model predicts the force-displacement hysteretic relationship with reasonable accuracy. But discrepancies also exist; the main difference may be caused by residual stress and the lack of stiffeners; thus, more experimental and finite element research studies are needed to establish the more accurate formulas of the force-displacement hysteretic relationships.

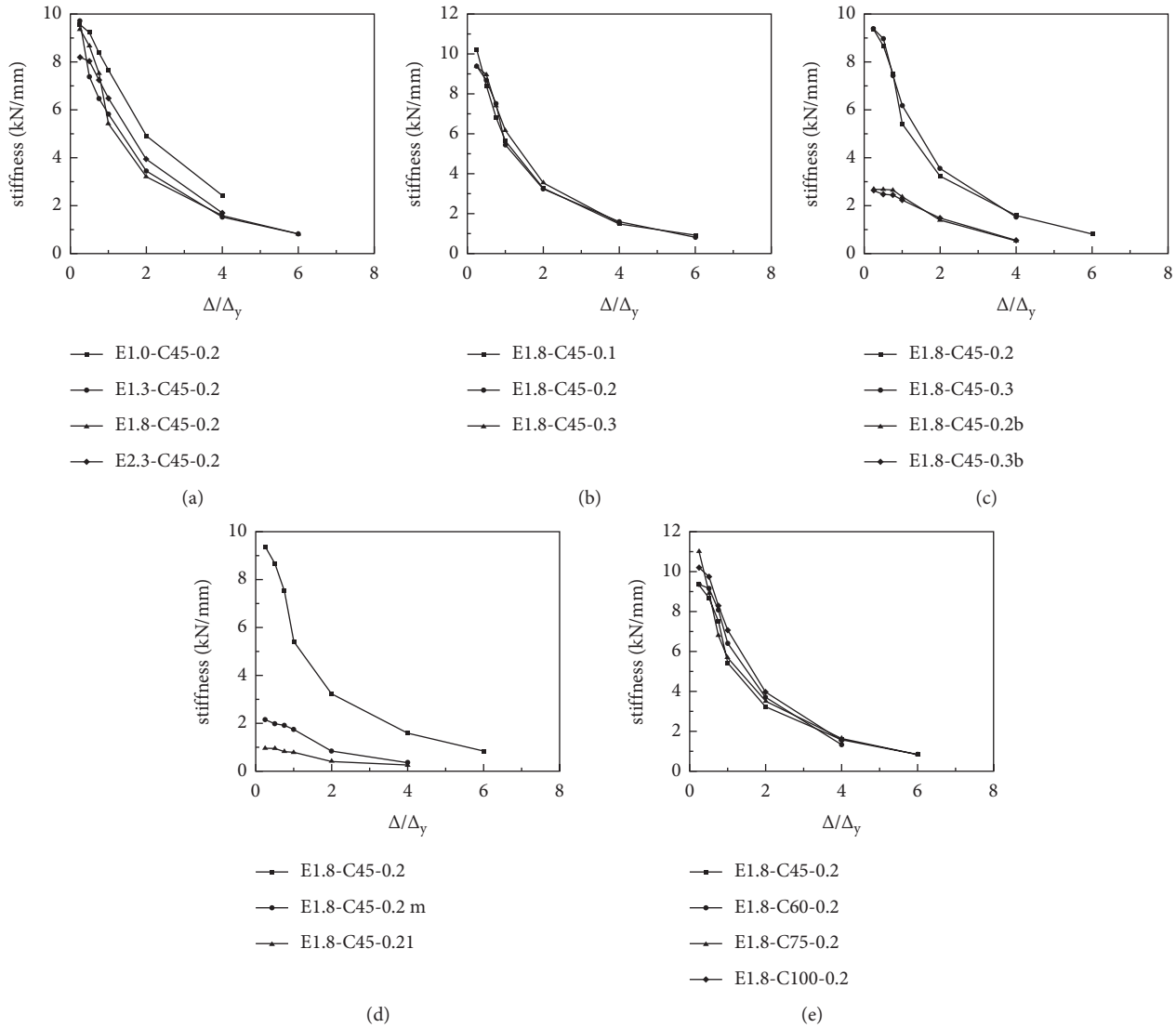

Figure 11: Stiffness of test specimens. (a) Variation of aspect ratio. (b) Variation of axial compression ratio. (c) Variation of bending axis. (d) Variation of slenderness ratio. (e) Variation of concrete strength.

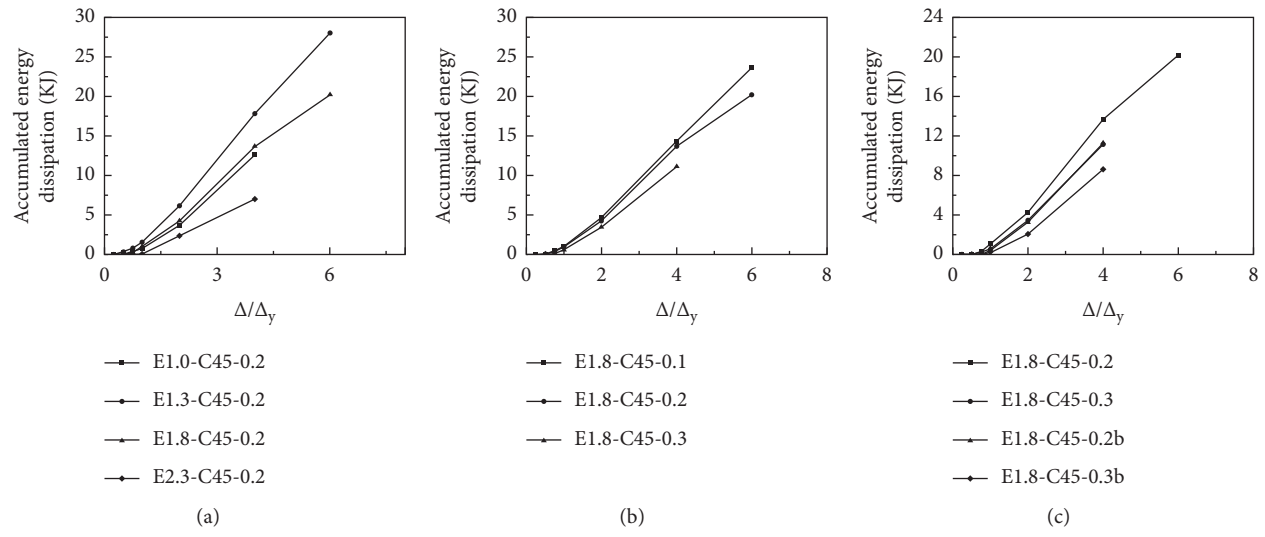

Figure 12: Continued.

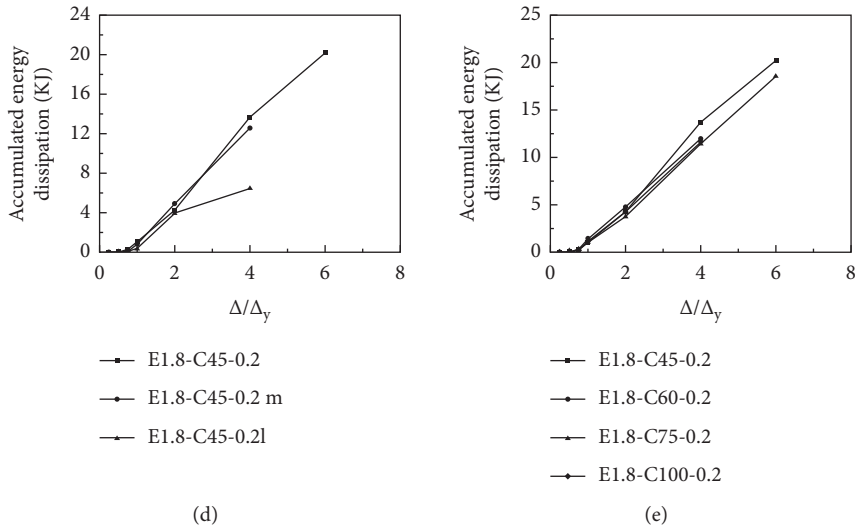

Figure 12: Accumulated energy dissipation of test specimens. (a) Variation of aspect ratio. (b) Variation of axial compression ratio. (c) Variation of bending axis. (d) Variation of slenderness ratio. (e) Variation of concrete strength.

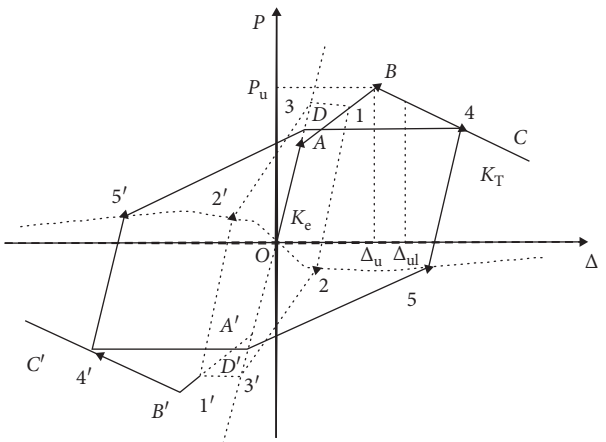

Figure 13: Simplified force-displacement relationship.

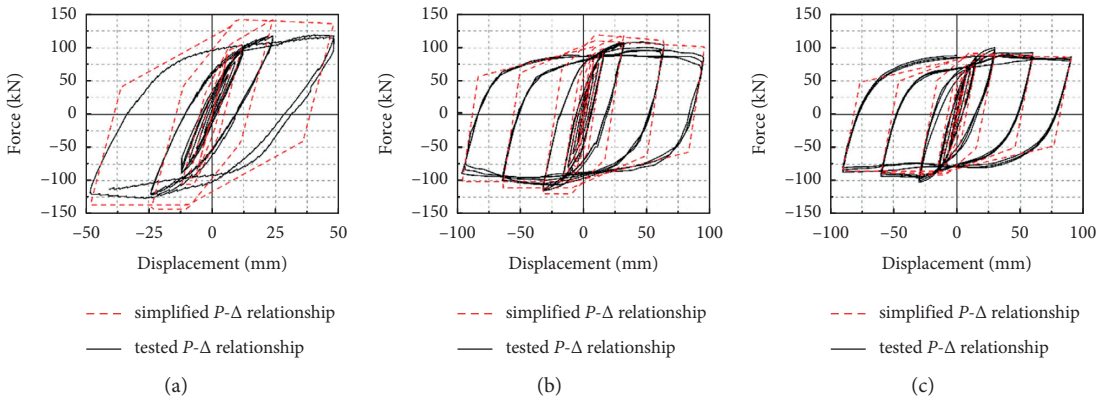

Figure 14: Continued.

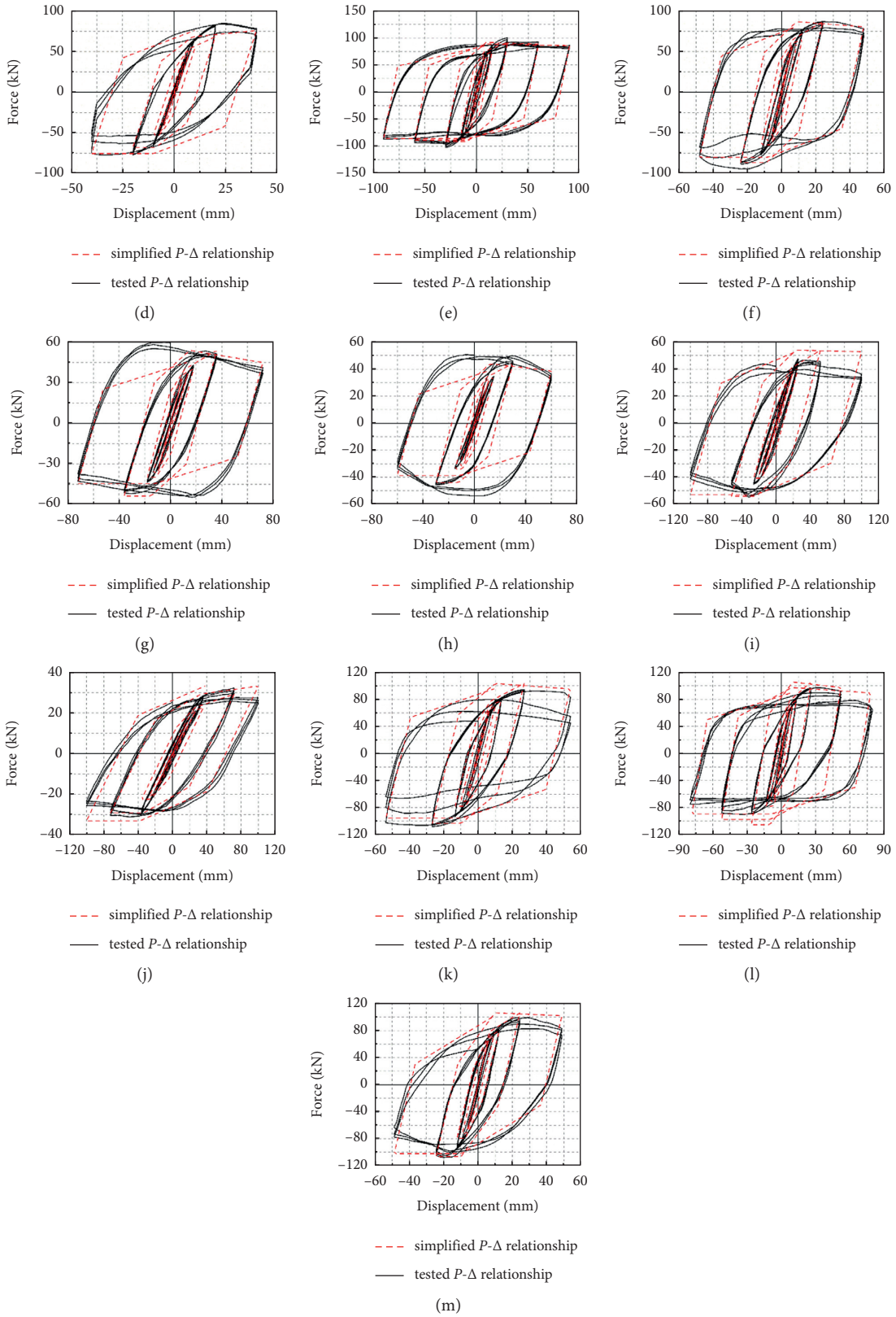

Figure 14: Comparison of simplified P-Δ relationship with tested P-Δ relationship. (a) E1.0-c45-0.2. (b) E1.3-c45-0.2. (c) E1.8-c45-0.2. (d) E2.3-c45-0.2. (e) E1.8-c45-0.1. (f) E1.8-c45-0.3. (g) E1.8-c45-0.2b. (h) E1.8-c45-0.3b. (i) E1.8-c45-0.2m. (j) E1.8-c45-0.2l. (k) E1.8-c60-0.2. (l) E1.8-c75-0.2. (m) E1.8-c100-0.2.

5. Conclusions

This study has focused on the seismic performance of elliptical CFST beam-columns under combined axial compression and cyclic lateral load. The main conclusions are summarized as follows:

(1) Most of the specimens fail in local buckling, but there are individual specimens that failed in abrupt fracture of the steel tube, which reveals the stiffeners must be used at the column base.

(2) The horizontal load and displacement hysteretic curves of all specimens are chubbiness without obvious pinching. Almost all specimens show good plastic deformation capacity and energy dissipation performance, which indicate that the elliptical CFST beam-column has good seismic performance, and it can be applied in the seismic area.

(3) The ultimate loads increase with the increasing concrete strength, but decrease with the increasing aspect ratio, axial compression ratio, and slenderness ratio. The ultimate load of major axis bending specimens is notably larger than that of minor axis bending specimens.

(4) The ductility index decreases with the increasing concrete strength, axial compression ratio, and slenderness ratio. The ductility index of major axis bending specimens is notably larger than that of minor axis bending specimens. The aspect ratio seems to have no markable influence on ductility index.

(5) The energy dissipation capacity increases with the decreasing aspect ratio, concrete strength, axial compression ratio and slenderness ratio. The energy dissipation capacity of major axis bending specimens is significantly larger than that of minor axis bending specimens.

(6) The simplified trilinear force-displacement model proposed by Han [2, 32] for rectangular and circular CFST beam-columns is also suitable for predicting the force-displacement hysteretic relationship of elliptical CFST beam-columns.

(7) Further studies on the seismic performance of elliptical CFST should conduct for design and engineering practice, including the influence of residual stress, the modified force-displacement model, and detailed parametric analysis.

Data Availability

The data used to support the findings of this study are available from the corresponding author upon request.

Conflicts of Interest

The authors declare that they have no conflicts of interest.

Acknowledgments

This research was financially supported by the Fundamental Research Funds for Quzhou University (BSYJ202012) and the Zhejiang Provincial Natural Science Foundation (LY18E080014).

References

[1] L.-H. Han, W. Li, and R. Bjorhovde, "Developments and advanced applications of concrete-filled steel tubular (CFST) structures: Members," *Journal of Constructional Steel Research*, vol. 100, pp. 211–228, 2014.

[2] L. H. Han, *Concrete Filled Steel Tubular Structures——Theory and Practice*, China Science Publishing & Media Ltd, Beijing, China, 3th edition, 2016.

[3] H. Yang, D. Lam, and L. Gardner, "Testing and analysis of concrete-filled elliptical hollow sections," *Engineering Structures*, vol. 30, no. 12, pp. 3771–3781, 2008.

[4] X. L. Zhao and J. A. Packer, "Tests and design of concrete-filled elliptical hollow section stub columns," *Thin-Walled Structures*, vol. 47, no. 6-7, pp. 617–628, 2009.

[5] N. Jamaluddin, D. Lam, X. H. Dai, and J. Ye, "An experimental study on elliptical concrete filled columns under axial compression," *Journal of Constructional Steel Research*, vol. 87, pp. 6–16, 2013.

[6] T.-M. Chan, Y.-M. Huai, and W. Wang, "Experimental investigation on lightweight concrete-filled cold-formed elliptical hollow section stub columns," *Journal of Constructional Steel Research*, vol. 115, pp. 434–444, 2015.

[7] Y. Cai, W.-M. Quach, M.-T. Chen, and B. Young, "Behavior and design of cold-formed and hot-finished steel elliptical tubular stub columns," *Journal of Constructional Steel Research*, vol. 156, pp. 252–265, 2019.

[8] X. X. Zha, G. B. Gong, and X. C. Liu, "Study on behavior of concrete filled elliptical steel tube members part I: short and long columns under axial compression," *Adv. Steel Constr.*vol. 9, no. 2, pp. 90–107, 2013.

[9] K. Uenaka, "Experimental study on concrete filled elliptical/oval steel tubular stub columns under compression," *Thin-Walled Structures*, vol. 78, pp. 131–137, 2014.

[10] S. Yi and B. Young, "Experimental investigation of concrete-filled cold-formed steel elliptical stub columns," in *Proceedings of the 16th International Symposium for Tubular Structures*, Melbourne, Australia, December, March 2017.

[11] F. Liu, Y. Wang, and T.-m. Chan, "Behaviour of concrete-filled cold-formed elliptical hollow sections with varying aspect ratios," *Thin-Walled Structures*, vol. 110, pp. 47–61, 2017.

[12] Y. W. Xu, J. Yao, and X. Sun, "Cold-formed elliptical concrete-filled steel tubular columns subjected to monotonic and cyclic axial compression," *Advances in Structural Engineering*, vol. 23, no. 7, pp. 1383–1396, 2020.

[13] T. Sheehan and X. H. Dai, T. M. Chan and T. M. Chan, Structural response of concrete-filled elliptical steel hollow sections under eccentric compression," *Engineering Structures*, vol. 45, pp. 314–323, 2012.

[14] X. X. Zha, G. B. Gong, and X. C. Liu, "Study on behavior of concrete filled elliptical steel tube members part 2: under bending and eccentric compression," *Adv. Steel Constr.*vol. 9, no. 2, pp. 108–123, 2013b.

[15] Q.-X. Ren, L.-H. Han, D. Lam, and W. Li, "Tests on elliptical concrete filled steel tubular (CFST) beams and columns," *Journal of Constructional Steel Research*, vol. 99, pp. 149–160, 2014.

[16] W. Qiu, *Beam-column behaviour of concrete-filled elliptical hollow sections*, Ph.D. Dissertation, Imperial College London, London, UK, 2017.

[17] H. Yang, F. Q. Liu, T. M. Chan, and W. Wang, "B ehaviours of concrete-filled cold-formed elliptical hollow section beam-columns with varying aspect ratios," *Thin-Walled Structures*, vol. 120, pp. 9–28, 2017.

[18] X. Dai and D. Lam, "Numerical modelling of the axial compressive behaviour of short concrete-filled elliptical steel columns," *Journal of Constructional Steel Research*, vol. 66, no. 7, pp. 931–942, 2010.

[19] X. H. Dai, D. Lam, N. Jamaluddin, and J. Ye, "Numerical analysis of slender elliptical concrete filled columns under axial compression," *Thin-Walled Structures*, vol. 77, pp. 26–35, 2014.

[20] W. Qiu, F. McCann, A. Espinos, M. L. Romero, and L. Gardner, "Numerical analysis and design of slender concrete-filled elliptical hollow section columns and beam-columns," *Engineering Structures*, vol. 131, pp. 90–100, 2017.

[21] J. F. Wang, Q. H. Shen, H. Jiang, and X. B. Pan, "Analysis and design of elliptical concrete-filled thin-walled steel stub columns under axial compression," *Int. J. Steel Struct.*vol. 18, no. 2, pp. 365–380, 2018.

[22] M. Ahmed and Q. Q. Liang, "Computational simulation of elliptical concrete-filled steel tubular short columns including new confinement model," *Journal of Constructional Steel Research*, vol. 174, Article ID 106294, 2020.

[23] X. F. Ma, "Research on seismic performance test and calculation methods of elliptical concrete filled steel tube," Master Dissertation, Hefei University of Technology, Hefei, China, 2019.

[24] C. Fang, F. Zhou, Z. Y. Wu, and F. C. Wang, "Concrete-filled elliptical hollow section beam-columns under seismic loading," *Journal of Structural Engineering*, vol. 146, no. 8, Article ID 04020144, 2020.

[25] Z. Y. Chen, J. Q. Zhu, and P. G. Wu, *High Strength concrete and its Application*, Tsinghua University Press Ltd, Beijing, China, 1992.

[26] Gb/T. 228.1-2010, *Metallic Materials-Tensile Testing-Part 1: Method of Test at Room Temperature*, China Standard Press, Beijing, China, 2010.

[27] Jgj/T 101, *Specification for Seismic Test of Buildings*, China Architecture & Building Press, Beijing, China, 2015.

[28] X. Z. Zhao, F. P. Wen, Y. Y. Chen et al., "Experimental study on the static performance of steel reinforced concrete columns with high encased steel ratios," *Struct Des Tall Spec*, vol. 27, no. 15, p. e1536, 2018.

[29] Y. B. Wu, "The experimental study of concealed bracings impact on seismic behavior of steel high-strength concrete low shear walls," Master Dissertation,, Chongqing University, Chongqing, China, 2011.

[30] C. Fang, F. Zhou, and W. Wu, "Performance of elliptical hollow sections under combined compression and cyclic bending," *Journal of Structural Engineering*, vol. 144, no. 8, Article ID 04018102, 2018.

[31] C. Fang, F. Wang, C. Wang, and Y. Zheng, "Cyclic behavior of oval hollow section (OHS) beam-columns," *Thin-Walled Structures*, vol. 161, Article ID 107430, 2021.

[32] L.-H. Han and Y.-F. Yang, "Cyclic performance of concrete-filled steel CHS columns under flexural loading," *Journal of Constructional Steel Research*, vol. 61, no. 4, pp. 423–452, 2005.

[33] ACI, *Building code requirements for structural concrete and commentary*, American Concrete Institute, Farmington Hills, MI, USA, 2011.